ADVANCED FUNCTIONAL MATERIALS
www.afm-journal.de

Mitigating Detrimental Effect of Self-Doping Near the Anode in Highly Efficient Organic Solar Cells

Yong Ryun Kim, Oskar J. Sandberg, Stefan Zeiske, Gregory Burwell, Drew B. Riley, Paul Meredith, and Ardalan Armin**

Poly(3,4-ethylenedioxythiophene):polystyrene sulfonate (PEDOT:PSS) has been one of the most established hole transport layers (HTL) in organic solar cells (OSCs) for several decades. However, the presence of PSS$^-$ ions is known to deteriorate device performance via a number of mechanisms including diffusion to the HTL-active layer interface and unwanted local chemical reactions. In this study, it is shown that PSS$^-$ ions can also result in local *p*-doping in the high efficiency donor:non-fullerene acceptor blends – resulting in photocurrent loss. To address these issues, a facile and effective approach is reported to improve the OSC performance through a two-component hole transport layer (HTL) consisting of a self-assembled monolayer of 2PACz ([2-(9H-Carbazol-9-yl)ethyl]phosphonic acid) and PEDOT:PSS. The power conversion efficiency (PCE) of 17.1% using devices with PEDOT:PSS HTL improved to 17.7% when the PEDOT:PSS/2PACz two-component HTL is used. The improved performance is attributed to the overlaid 2PACz layer preventing the formation of an intermixed *p*-doped PSS$^-$ ion rich region (≈5–10 nm) at the bulk heterojunction-HTL contact interface, resulting in decreased recombination losses and improved stability. Moreover, the 2PACz monolayer is also found to reduce electrical shunts that ultimately yield improved performance in large area devices with PCE enhanced from 12.3% to 13.3% in 1 cm^2 cells.

1. Introduction

Organic solar cells (OSCs) have seen intense research and development efforts in the past decades as a potential energy conversion technology, owing to their benefits of light weight, low cost, easy preparation, and printability. The state-of-the art power conversion efficiencies (PCEs) of OSCs have recently approached nearly 19% in single-junction and 20% in tandem structures.[1–4] This has partly been driven by a tremendous progress in device physics, development of polymer donor and non-fullerene acceptors (NFAs), device optimization (morphology), and improved device structures.[4–7] Going forward, to break the 20% efficiency limit and approach the optimistic 25% predicted values, all minor and major loss channels in the bulk and interfaces must be identified and mitigated to any possible extent.[8] NFA-based OSCs have now demonstrated promising optical and electrical figures of merits with strongly reduced bulk recombination being reported.[9,10] Interface engineering becomes particularly important in the case of systems with strongly reduced bimolecular recombination, in which case the carrier density including minority carrier densities is large at the contacts.[11–14] For example, an interfacial film between the bulk heterojunction (BHJ) active layer and the electrodes can substantially improve the selective collection of photogenerated electrons and holes by reducing undesired energy barriers at the contact interface.

For conventional device architectures, a hole transport layer (HTL) is inserted between the indium tin oxide (ITO) and the BHJ active layer. Poly (3,4-ethylenedioxythiophene):polystyrene sulfonate (PEDOT:PSS) remains the standard HTL for the highest efficiency OSC devices due to its advantages of commercial accessibility, low temperature processing from water-based solution, good film formation, and outstanding optical transparency.[15–17] However, PEDOT:PSS has several drawbacks such as relatively low conductivity (10^{-3}–10^{-4} Scm^{-1}) and poor operational stability due to the presence of PSS$^-$ ions, which not only limits the device performance but also may induce unwanted reactions (e.g., etch both underlying ITO electrode and BHJ active layer) in the conventional structure.[18–21] Moreover, the presence of PSS$^-$ ions may result in the formation of an intermixed region at the interface between the HTL and BHJ active layer, possibly giving rise to detrimental effects on the device performance.[22] Regrettably, the presence of PSS$^-$ ions is unescapable in this system due to solubility chemistry and the fact that the ion is a substantial control factor in the

---

Y. R. Kim, O. J. Sandberg, S. Zeiske, G. Burwell, D. B. Riley, P. Meredith, A. Armin
Sustainable Advanced Materials (Sêr-SAM)
Department of Physics
Swansea University
Singleton Park, Swansea SA2 8PP Wales, UK
E-mail: o.j.sandberg@swansea.ac.uk; ardalan.armin@swansea.ac.uk

The ORCID identification number(s) for the author(s) of this article can be found under https://doi.org/10.1002/adfm.202300147.

DOI: 10.1002/adfm.202300147

underlying conductivity mechanism. As a result, there is a need for novel alternative HTLs with improved properties for both advancing basic efficiency metrics and for scaling and stability considerations. One strategy to form high performance HTLs is the use of self-assembled monolayers (SAMs).

SAMs have gained significant attention in perovskite (PVSK) and OSCs as new HTL candidates to replace PEDOT:PSS including numerous solution processable oxides (NiO_x, MoO_x, and WO_3).[23–29] Recent studies using derivatives of [2-(9*H*-Carbazol-9-yl)ethyl]phosphonic acid (2PACz), have demonstrated high device performances in single-junction OSCs (≈18%) and PVSK cells (≈21%), as well as in silicon (Si)/PVSK tandem device structures (≈29%).[13,14,30–35] However, it has been reported that due to the sensitive chemical structure of SAM materials, conformal layer coverage on the ITO is difficult to achieve. The quality of the conformal SAM layer depends on both the intrinsic properties of the ITO and the pre-treatment of the ITO surface.[30,36–38] Besides, the surface coverage is critical because poor coverage induces large losses in photovoltaic parameters, and increases the likelihood of deleterious electrical shunts. As the approach of using SAMs as HTLs is yet to be fully implemented, it is imperative to find other HTLs or alternative approaches to overcome these coverage issues.

In this article, we introduce a two-component HTL consisting of PEDOT:PSS/2PACz in conventional structure OSCs. We use OSCs based on a donor:NFA blend of poly[(2,6-(4,8-bis(5-(2-ethylhexyl-3-fluoro)thiophen-2-yl)-benzo[1,2-b:4,5-b′]dithiophene))-alt-(5,5-(1′,3′-di-2-thienyl-5′,7′-bis(2-ethylhexyl)benzo[1′,2′-c:4′,5′-c′]dithiophene-4,8-dione)] (PM6) and 2,2′- [[12,13-Bis(2-butyloctyl)-12,13-dihydro-3,9-dinonylbisthieno[2⁗,3⁗:4″,5″]thieno[2″,3″:4,5]pyrrolo[3,2-e:2″,3″-g][2,1,3]benzothiadiazole-2,10-diyl]bis[methylidyne(5,6-chloro-3-oxo-1H-indene-2,1(3H)-diylidene)]]bis[propanedinitrile] (BTP-eC9) as model systems. PM6:BTP-eC9 OSCs with a two-component PEDOT:PSS/2PACz HTL exhibited an improved device performance with the highest PCE of 17.7%, as compared to the OSCs with a PEDOT:PSS HTL (17.1%). Additionally, OSCs with two-component HTLs showed higher reproducibility (≈17% in 0.036 cm^2 and 13% in 1 cm^2). These results were found to be applicable to other NFA systems as well. Besides, the OSCs with two-component PEDOT:PSS/2PACz HTL displayed improved stability in both continuous photo-irradiation and air measurements. We provide evidence suggesting that the deposition of a conformal 2PACz layer on PEDOT:PSS prevents the formation of a few nanometer (≈5–10 nm) thick intermixed region consisting of PSS^- ions in the BHJ active layer at the interface. This leads to an improvement in both the device efficiency and stability, suggesting an approach toward driving the 20% OSC target.

2. Results and Discussion

In this study OSCs with two-component HTLs based on PEDOT:PSS/2PACz, using a conformal 2PACz layer to passivate the acidic PEDOT:PSS surface, were investigated. To this end, we fabricated conventional OSC devices with a configuration of ITO/HTL/PM6:BTP-eC9/PNDIT-F3N-Br/Ag as shown in **Figure 1**a. All chemical abbreviations are provided

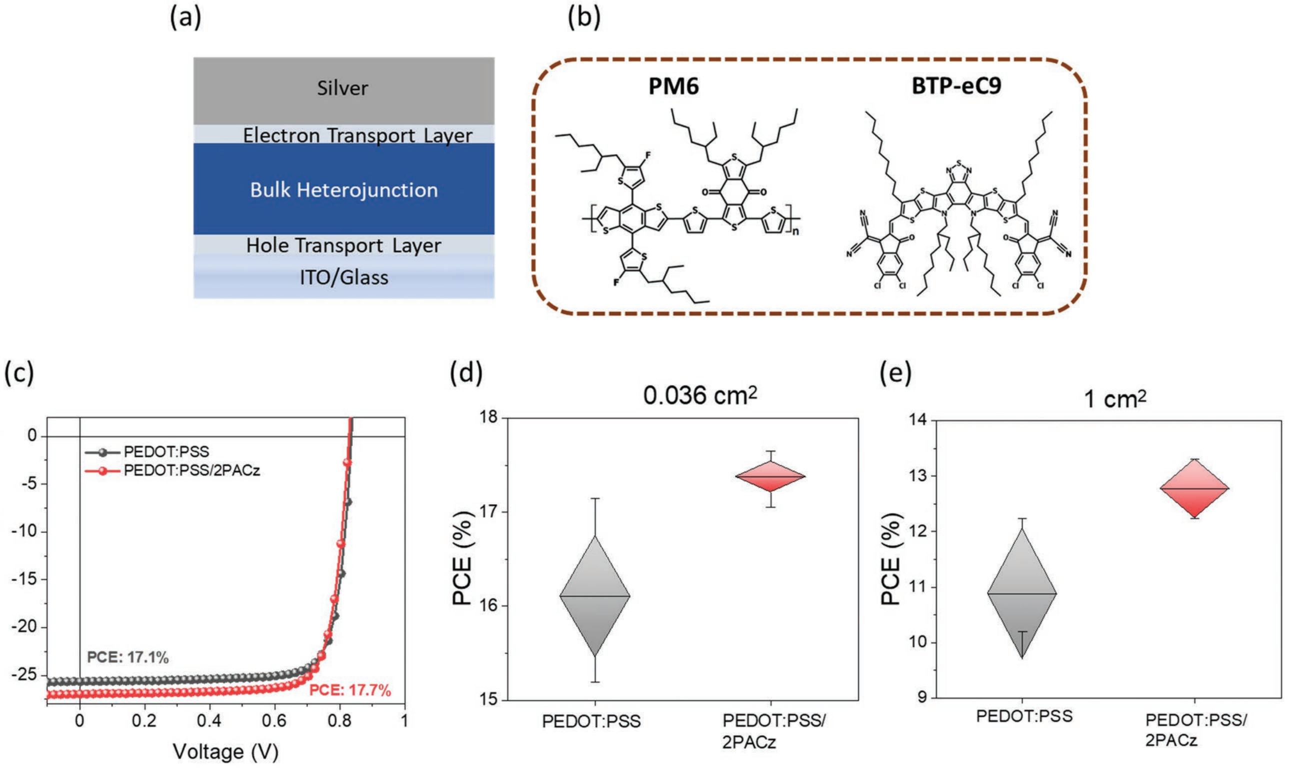

Figure 1. a) Device structure of the OSC with conventional architecture. b) The chemical structure of PM6 and BTP-eC9 used as the BHJ active layer. c) The current density–voltage (*J*–*V*) curves of hero PM6:BTP-eC9 OSCs with different HTLs. d) PCE of small-area devices (0.036 cm^2) obtained from 20 devices and e) of large-area devices (1 cm^2) from a batch with 5 devices.

Table 1. Photovoltaic parameters of OSCs based on PM6:BTP-eC9 with different HTLs under 1 sun illumination of AM1.5G, ≈100 mW cm^{-2}. The average parameters were calculated from 20 devices with an aperture area of 0.036 cm^2.

HTL	V_{oc} [V]	J_{sc} [mA cm^{-2}]	FF [%]	PCE [%]	Integrated J_{sc} [mA cm^{-2}]
PEDOT:PSS	0.84 (0.83 ± 0.012)	25.7 (24.8 ± 0.7)	80.0 (78.6 ± 1.4)	17.1 (16.1 ± 0.6)	24.5
PEDOT:PSS/2PACz	0.83 (0.83 ± 0.004)	26.9 (25.5 ± 0.6)	79.1 (79.8 ± 0.7)	17.7 (17.4 ± 0.1)	25.3

in the Experimental section. The optimized HTL thickness of PEDOT:PSS and two-component PEDOT:PSS/2PACz were 27.5 and 29.7 nm, respectively, as measured by spectroscopic ellipsometry (see Figure S1, Supporting Information), suggesting that the thickness of the 2PACz layer on PEDOT:PSS was below 1.8 nm. The molecular structures of PM6 and BTP-eC9, used as donor and acceptor, respectively, in the BHJ active layer are shown in Figure 1b. Further details of the device fabrication are provided in the Experimental section.

Figure 1c shows the hero current density–voltage (*J*–*V*) characteristics of OSCs measured under standard AM1.5G illumination at 100 mW cm^{-2}. For OSCs with PEDOT:PSS HTL, a highest PCE of 17.1% was obtained, with corresponding short-circuit current density (J_{sc}) of 25.7 mA cm^{-2}, open-circuit voltage (V_{oc}) of 0.84 V, and fill factor (FF) of 80%. The obtained photovoltaic parameters agree with values reported in the literature.[9] On the other hand, OSCs with two-component PEDOT:PSS/2PACz HTL yielded higher performance, with the champion device showing a PCE of 17.7%, a J_{sc} of 26.9 mA cm^{-2}, V_{oc} of 0.83 V, and FF of 79%. The J_{sc} values obtained from the *J*–*V* characteristics match well with integrated J_{sc} values within an approximate error of 5% calculated from the integrated external quantum efficiency (EQE) spectra as shown in Figure S2 (Supporting Information). Moreover, from statistical photovoltaic performances from 20 devices (Figure 1d; Figure S3, Supporting Information), the OSCs with two-component PEDOT:PSS/2PACz HTL show an excellent reproducibility with a much narrower PCE distribution and higher average PCE (17.4%) compared to devices with PEDOT:PSS only (16.1%). Thus, our approach potentially improves the aforementioned conformal deposition problems of SAM layers on ITO substrates. **Table 1** summarizes the device performance data of all OSC devices.

The enhanced device performance obtained with two-component PEDOT:PSS/2PACz mainly stems from a significant increment of the J_{sc} (from 25.7 to 26.9 mA cm^{-2}), although displaying a slightly smaller V_{oc} (0.84–0.83 V). Furthermore, from the corresponding dark *J*–*V* curves, we found that the dark current in reverse bias is one order of magnitude lower in OSCs with two-component PEDOT:PSS/2PACz HTL (see Figure S4, Supporting Information). This suggests that PEDOT:PSS/2PACz HTL displays smaller leakage currents and larger shunt resistance, expected to be beneficial for large area devices. In this regard, we also fabricated a 5-batch of 1 cm^2 device-area OSCs with different HTLs (see Figure 1e). OSCs with two-component PEDOT:PSS/2PACz demonstrate excellent PCEs up to 13.3%, whereas OSCs with PEDOT:PSS demonstrate PCEs below 12.2%.

To clarify the origin of the enhanced OSC performance obtained with two-component PEDOT:PSS/2PACz HTLs, we next characterized and compared the properties of the different ITO/HTL substrates. **Figure 2**a shows the chemical structures of

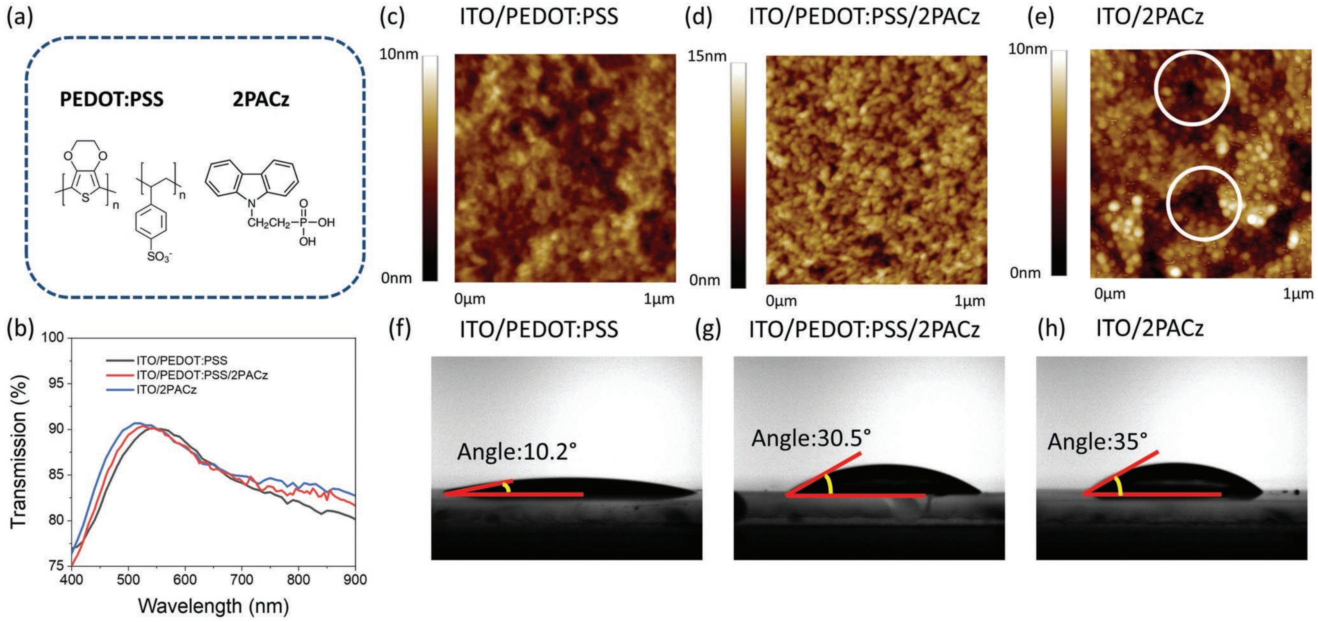

Figure 2. a) Chemical structure and b) transmittance versus wavelength spectra of PEDOT:PSS, PEDOT:SS/2PACz and 2PACz films deposited on ITO substrates. c–e) AFM and f–h) water contact angle images of PEDOT:PSS, PEDOT:PSS/2PACz, and 2PCAz, respectively. White circles in (e) indicate possible pinholes.

PEDOT:PSS and 2PACz. The measured transmittance spectra of PEDOT:PSS, two-component PEDOT:PSS/2PACz, and 2PACz on ITO are shown in Figure 2b. All three of the prepared films exhibited comparable high transparencies (peak ≈90%) within the relevant visible region. We note that the transmittance of the 2PACz is slightly higher than that of PEDOT:PSS below 500 nm and above ≈800 nm. Notably, the transmittance spectrum for two-component PEDOT:PSS/2PACz HTL generally lies in between the corresponding spectra of PEDOT:PSS and 2PACz across the considered wavelength range (400–900 nm).

Figure 2c–e shows the surface morphologies of the films (PEDOT:PSS, 2PACz, and two-component PEDOT:PSS/2PACz) assessed by atomic force microscopy (AFM). The morphology of PEDOT:PSS and 2PACz deposited on an ITO substrate is relatively smooth with the root-mean-square (RMS) roughness of 1.1 and 1.5 nm, respectively, while the RMS roughness of the two-component PEDOT:PSS/2PACz is 1.5 nm, which is same to neat 2PACz. The AFM images of two-component PEDOT:PSS/2PACz showed almost identical features to that of 2PACz deposited on ITO, indicative of full coverage of 2PACz over PEDOT:PSS. However, the 2PACz on ITO showed several valley features (Figure 2e white circle), indicative of possible pinholes that can cause severe electrical shunts or surface recombination. This is further supported by the relative changes in the Derjaguin–Muller–Toporov (DMT, reduced Young's modulus) of the films measured simultaneously with the surface potential data and morphology (see Figure S5, Supporting Information), consistent with previous reports.[39,40] In contrast, the two-component PEDOT:PSS/2PACz film has little variation in the DMT modulus across the scanned area, which would be consistent with the formation of a conformal 2PACz SAM film.

In principle, the surface properties of the HTL can change the morphology of the BHJ active layer.[41,42] To this end, water contact angle measurements, which is a simple and versatile method to determine the surface properties, were performed. The corresponding measurements are shown for PEDOT:PSS, two-component PEDOT:PSS/2PACz, and 2PACz on ITO substrates in Figure 2f–h. The PEDOT:PSS film possesses a typical hydrophilic surface with a water contact angle of 10.2° whereas the two-component PEDOT:PSS/2PACz film is more hydrophobic with a higher water contact angle of 30.5°. Such a small difference may have an impact on the wetting and drying dynamics during spin-coating of BHJ active layers. While we did not observe any differences in the morphologies of the BHJ active layer films, the increased hydrophobicity of PEDOT:PSS/2PACz is expected to reduce the presence of PSS$^-$ ions at the contact interface.

To further explore the elemental analysis of the PEDOT:PSS/2PACz surfaces, we next conducted X-ray photoelectron spectra (XPS) measurements. Signals characteristics of S 2*p* and P 2*p* peaks can be directly attributed to the presence of the PEDOT:PSS and 2PACz layers, respectively. **Figure 3**a,b show the high resolution XPS (HR-XPS) spectra of S 2*p* core levels for PEDOT:PSS, two-component PEDOT:PSS/2PACz and 2PACz films on ITO substrates. For films including PEDOT:PSS and two-component PEDOT:PSS/2PACz, the XPS bands between 168 and 164 eV are mainly attributed to the sulfonate moiety of PSS, whereas the XPS bands at between 164 and 160 eV can be attributed to the thiophene rings of PEDOT and have different chemical environments.[43,44] The fitted line illustrates that the intensity of the sulfonate peak was significantly reduced for the two-component PEDOT:PSS/2PACz film. The ratio of band area for PSS and PEDOT was used to calculate the relative composition of PSS to PEDOT at the surface. The calculated surface ratio of PSS to PEDOT for PEDOT:PSS with and without 2PACz is 7:1 and 12:1, respectively, which indicate that a large amount of sulfonate was washed off during the deposition of 2PACz on PEDOT:PSS. We calculated the ratio of the PEDOT/PSS structure in PEDOT:PSS from the peak area ratio of PEDOT and PSS, which are shadowed in color. We note, however, that the conductivity is

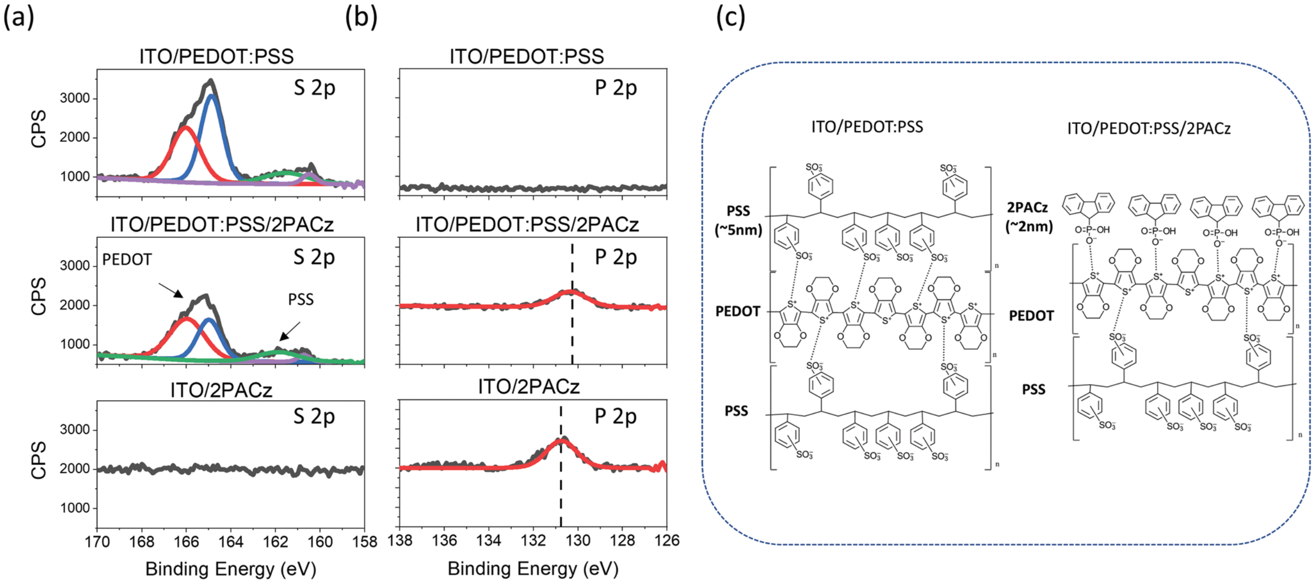

Figure 3. High resolution XPS patterns of the atomic core levels of a) S 2*p* and b) P 2*p* for the three different HTLs. c) Schematic illustration of the film structure in PEDOT:PSS and PEDOT:PSS/2PACz.

slightly higher for two-component PEDOT:PSS/2PACz films (see Figure S6, Supporting Information). In addition, the peak corresponding to the core level of P 2*p* from two-component PEDOT:PSS/2PACz is directly attributed to the presence of the 2PACz on PEDOT:PSS film (Figure 3b). Note that the binding energy of P 2*p* peak for two-component PEDOT:PSS/2PACz shifts toward lower binding energy (0.5 eV) after deposition of 2PACz. This chemical shift indicates that the O atoms in phosphorus (P—O) of 2PACz contribute lone pairs of electrons to the S atom in the thiophene ring of PEDOT, thus strongly anchoring the bond of P—O—S at the interface (Figure 3c).[45]

Finally, we examine and compare the work functions (WF) of the different HTL substrates. Ultraviolet photoelectron spectroscopy (UPS) was conducted as shown in Figure S7 (Supporting Information). The energy levels calculated from the UPS data are summarized in Table S1 (Supporting Information). The resulting data suggest WF values of 5.0, 5.4, and 5.5 eV for PEDOT:PSS, two-component PEDOT:PSS/2PACz, and 2PACz, respectively, all higher than the WF of ITO (4.7 eV). For comparison, we also performed Kelvin probe force microscopy (KPFM) measurements. The corresponding results of the contact potential difference (CPD) are shown in Figure S8a–c (Supporting Information). The KPFM measurements reveal WF values of 5.2 and 5.4 eV for PEDOT:PSS and two-component PEDOT:PSS/2PACz, respectively, which are in good agreement with the results obtained from UPS measurements and recent reports in the literature.[13,14] We stress, however, that owing to the uncertainties associated with these measurements, these results should be regarded as indicative rather than absolute. Nevertheless, the higher WF of PEDOT:PSS/2PACz suggests more favorable energetics as an HTL in general.

Based on the experimental results presented in Figures 2 and 3, the two-component PEDOT:PSS/2PACz HTL substrate differs from the PEDOT:PSS HTL in three main aspects which, in principle, could contribute to the improved overall device performance. The two-component PEDOT:PSS/2PACz has: i) a slightly red-shifted transmittance, ii) a higher WF, and iii) a more hydrophobic surface with a reduced amount of PSS$^-$ ions at the surface. To clarify the influence of these aspects in fully operational OSC devices, we next turn to electro-optical device simulations. In this regard, a numerical drift-diffusion (DD) model was used, which accounts for optical effects through an optical transfer-matrix model (TMM). The details of the DD and TMM have been published elsewhere.[46,47] For the DD simulations, we assume the bulk properties of the active layer to remain the same, using measured mobilities and recombination coefficients from previous work as input parameters.[9] A list of input parameters is provided in Table S2 (Supporting Information).

We first investigated whether optical differences between the substrates translate into noticeable differences in the photocurrent of OSCs. To this end, we conducted TMM simulations to calculate the photogeneration rate in the active layer, using experimentally determined optical constants of all layers in the full device stack as input. The refractive indices and extinction coefficients of the two HTLs (measured with ellipsometry) are shown in Figure S1 (Supporting Information). The corresponding *J*–*V* curves of OSCs are simulated in Figure S9 (Supporting Information). The introduction of a monolayer of 2PACz on PEDOT:PSS (PEDOT:PSS/2PACz) was found to only induce marginal changes in the photogeneration rate in the active layer and not enough to explain the improved J_{sc}.

Next we explored how the *J*–*V* curves are influenced by different energy offsets at the anode-side contact (see **Figure 4**a), with the associated energy offset being given by the difference between the WF at HTL contact and the hole transport level of the active layer. Increasing the energy offset (i.e., decreasing WF) resulted in an overall shift of the *J*–*V* curve toward smaller voltages and lower V_{oc} while keeping constant J_{sc}. This is a consequence of the concomitant reduction of the built-in voltage in the active layer and increase of surface recombination losses.[48–50] Comparing with the experimental *J*–*V* curves in Figure 1, we see that the experimentally observed behavior is very different, with the V_{oc} instead decreasing with PEDOT:PSS/2PACz but J_{sc} increases. These results indicate that an improved WF with 2PACz monolayer is not responsible for the enhanced OSC performance, and that optimal energy alignment at the HTL is likely already achieved with PEDOT:PSS in this BHJ system.

Finally, we modeled the effects of a more hydrophobic surface and a reduced amount of PSS$^-$ on the surface. A change in surface properties could, in principle, induce differences in the active layer thickness. The effect of varying the active layer thicknesses between 80 and 110 nm is simulated in Figure 4b. It can be seen that while increasing the active layer thicknesses results in a lower J_{sc} within this thickness range, the V_{oc} remains unchanged. The presence of PSS$^-$ ions at the surface, on the other hand, may result in the formation of a PSS$^-$ ions rich intermixed region in the BHJ active layer near the HTL interface.[22] Because of their negative space charge, PSS$^-$ ions effectively act as a *p*-type dopant within this region. Figure 4c demonstrates the effect of varying the width of a PSS$^-$ ion rich region. The presence of PSS$^-$ ions increases the hole conductivity of the active layer near at the HTL interface; however, this comes at the cost of an increased non-geminate recombination (as explained below), manifested in subsequent losses in the J_{sc}. Coincidentally, the presence of a *p*-doped region is also seen to give rise to a slightly increased V_{oc} in this case. These considerations suggest that the different experimental *J*–*V* curve behavior between OSCs with PEDOT:PSS/2PACz HTLs is due to suppression of a PSS$^-$ ion rich intermixed region near the HTL interface, explaining the experimentally observed increased J_{sc} and PCE and slightly reduced V_{oc} in these devices.

To substantiate the presence and suppression of a *p*-doped intermixed region in OSCs with PEDOT:PSS and PEDOT:PSS/2PACz, respectively, we conducted charge extraction by linearly increasing voltage (CELIV).[51,52] This technique allows for the thickness of the undoped region inside the active layer to be probed. In CELIV, a reverse-biased ramp up voltage is applied to the OSC in the dark, and the resulting transient current density response *j* is measured. The corresponding saturated current response (j_{sat}) reflects the thickness d_{eff} of the undoped region in the active layer via $j_{\mathrm{sat}} = \varepsilon\varepsilon_0 A/d_{\mathrm{eff}}$, where A is the voltage ramp up rate, ε the relative permittivity of the active layer, and ε_0 the vacuum permittivity.[53] Figure 4d shows the measured CELIV current transients, normalized to the geometric response, $j_0 = \varepsilon\varepsilon_0 A/d$, expected for an active layer with thickness $d = 100$ nm (assuming $\varepsilon = 4$). The inset of Figure 4d shows the corresponding simulated j/j_0 for the cases of a 10 nm

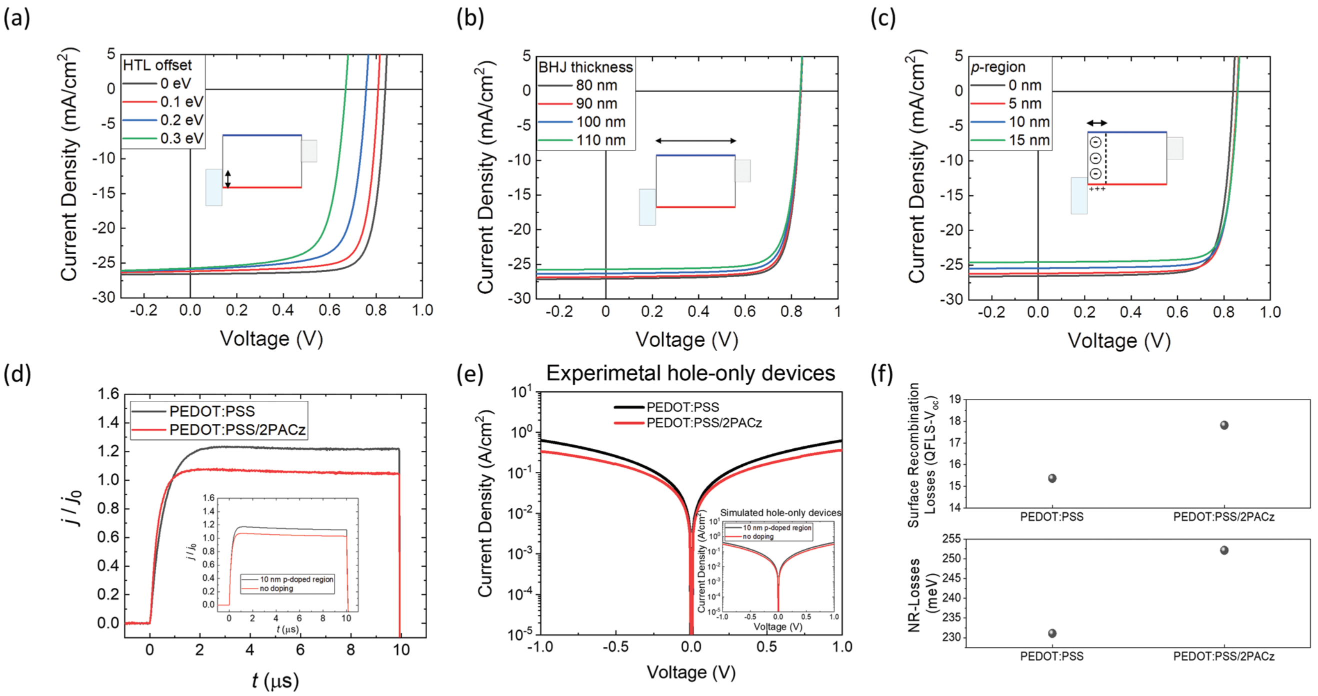

Figure 4. Upper panels show the simulated *J–V* characteristics for the case of a) varying energy level offset (hole injection barrier) at the anode contact (0 to 0.3 eV), b) varying active layer thickness (80 to 110 nm), and c) varying *p*-doped (PSS rich) region widths inside the active layer at the HTL interface (0 to 15 nm). In the lower panels: d) experimental normalized dark CELIV current transients j/j_0 as a function of time (t) for OSC devices with different HTLs, and e) *J–V* characteristics of hole-only ITO/HTL/PM6:BTP-eC9/MoOx/Ag devices; the insets in (d) and (e), respectively, show the corresponding simulations. f) shows EM-PLQY data for surface recombination losses (top) and total non-radiative (NR) losses (bottom).

thick *p*-doped region and no doping in the active layer. Indeed, devices with PEDOT:PSS/2PACz closely follow the behavior expected in case of an undoped active layer, while devices with PEDOT:PSS show larger j/j_0 consistent with a ≈10 nm thick *p*-doped intermixed region.

These findings are further corroborated by measured dark *J–V* characteristics of symmetric hole-only BHJ devices shown in Figure 4e. Larger injection currents are obtained for devices with a hole-injecting anode contact of PEDOT:PSS compared to devices with PEDOT:PSS/2PACz as the injecting anode contact. This behavior is consistent with the PEDOT:PSS case having of an additional thin *p*-doped region in the active layer near the anode contact, as simulated in the inset Figure 4e. We note that the PSS$^-$ ion rich intermixed region behaves like a virtual extension of the anode contact, effectively seen as a reduced active layer thickness in the dark. However, in contrast to OSCs with geometrically thinner active layers, which are expected to be accompanied with an increased J_{sc} (see Figure 4b), the presence of an intermixed region results in decreased J_{sc} consistent with the experiments. This is further supported by the active layer thicknesses measured by a profilometer showing no change.

Finally, the suppression of the intermixed region with PEDOT:PSS/2PACz is expected to result in an increased surface recombination loss in the V_{oc} (as explained below). To substantiate this, we conducted electro-modulated photoluminescence quantum yield (EM-PLQY) measurements to determine the difference between the quasi Fermi level splitting and V_{oc} in our devices.[54] This difference is a measure of the voltage loss due to the surface recombination, that is, due to the extraction of minority carriers. The corresponding analysis based on sensitive EQE and EM-PLQY measurements is shown in Figure 4f. Based on this analysis, we found that the reduced V_{oc} and corresponding increase in the non-radiative voltage loss (see Figure S10 and Table S3, Supporting Information), when changing the HTL from PEDOT:PSS to PEDOT:PSS/2PACz, is indeed associated with an increased surface recombination loss.

The above experimental findings, which are supported by theoretical calculations, suggest that for devices with PEDOT:PSS, the PSS can form a 5–10 nm thick intermixed region in the active layer, inducing a heavily *p*-doped interfacial region at the HTL/BHJ interface. This is demonstrated in **Figure 5**a,b, showing the corresponding simulated energy level diagrams of the active layer for the case with (PEDOT:PSS) and without (PEDOT:PSS/2PACz) a *p*-doped intermixed region, respectively. The corresponding charge collection efficiencies $\eta_{col}(x)$, as a function of the position x inside the active layer, are simulated in Figure 5c,d.[55] In the presence of the intermixed region, the high doping concentration gives rise to screening of the electric field inside this region. Subsequently, the charge collection of (minority) electrons generated within the intermixed region is dominated by diffusion, resulting in substantial recombination losses and decreased J_{sc}.[56] Notably, while this *p*-doped region is expected to enhance surface recombination of electrons inside this region, it prevents (minority) electrons generated outside this region from reaching the anode, since most electrons recombine within the *p*-doped region via bulk recombination before reaching the anode. In systems with suppressed bulk recombination (such as PM6:BTP-eC9), this

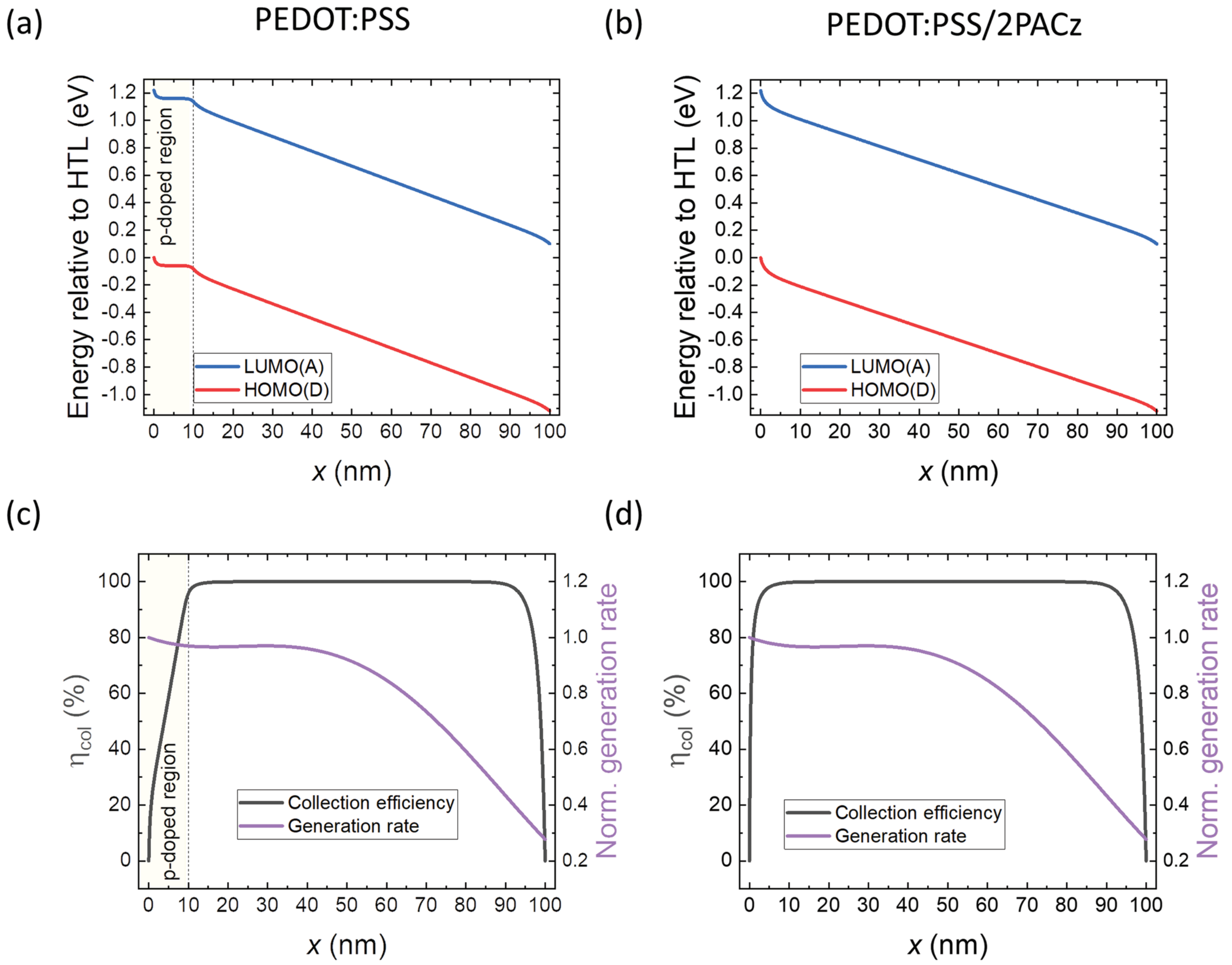

Figure 5. Simulated energy level diagrams of the active layer of an OSC at short circuit with a) a thin 10 nm *p*-doped region near the HTL (without 2PACz layer), and b) no doped region (with 2PACz layer on PEDOT:PSS). The LUMO levels of the acceptor and the HOMO levels of the donor are indicated by the blue and red solid lines, respectively. In (c) and (d) the respective simulated charge collection efficiencies, $\eta_{col}(x)$, as a function of the position *x* inside the active layer are shown. For comparison, the simulated (normalized) generation rate profiles of photogenerated charge carriers inside the active layer have been included.

ultimately reduces the overall surface recombination under open-circuit conditions, resulting in an increased V_{oc}.

We note that because of the complex BHJ morphology near the interface, however, the width of the PSS⁻ ion rich region is expected to be sensitive to small variations in the fabrication which can translate into relatively large device-to-device variations. This is reflected in the wide statistical variation in the PCE of OSCs with PEDOT:PSS HTLs. In contrast, depositing 2PACz on top of the PEDOT:PSS inhibits the formation of an intermixed region, resulting in a less *p*-doped or undoped interfacial region, and concomitantly larger values of J_{sc} and a considerably narrower PCE distribution for PM6:BTP-eC9 based OSCs.

The reduction of PSS⁻ ions at the surface is also anticipated to enhance the long-term stability of OSCs, which is an important factor for practical applications. As such, we further recorded operational stability and shelf-life stability measurements of encapsulated devices. The operational (shelf-life) stability was gauged under continuous one sun illumination (ambient) conditions. **Figure 6**a,b show the normalized PCEs of the devices with different HTLs when exposed to light and air as function of the time, respectively. OSCs with different HTLs showed different degrees of degradation during the operational stability measurements (see Figures S11 and S12, Supporting Information, for the details of other parameters). The degradation rate of OSCs with PEDOT:PSS is the fastest during the exposure time of 16 h, resulting in nearly a PCE that is 90% of its initial value. The poor stability limits the practical application of these devices. In contrast, the PCE of two-component PEDOT:PSS/2PACz exhibited greater stability and only reduced to a PCE of 96% of its initial value, suggesting that the incorporation of 2PACz layer between PEDOT:PSS and BHJ active layer enhanced the photo-stability. More interestingly, similar results can be found in the shelf-life stability measurements as seen in Figure 6b. The improvement in both stability measurements is attributed to the fact that the incorporation of 2PACz on

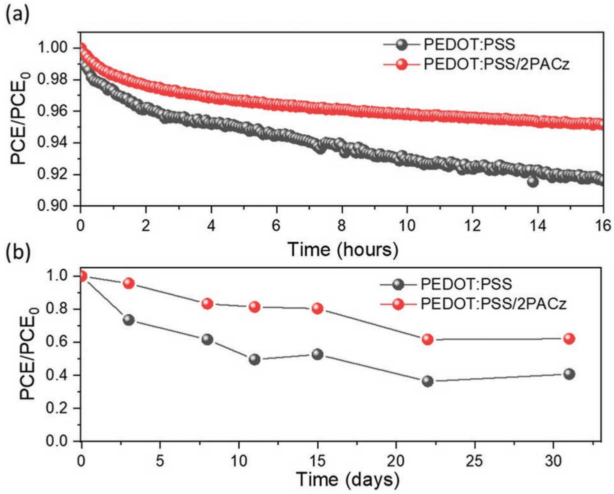

Figure 6. Normalized power conversion efficiency, as obtained a) under LED array (1 sun) continuous illumination in air and b) storing under ambient conditions (T = 25 °C and 20–40% relative humidity) in the dark, of encapsulated PM6:BTP-eC9 OSCs with different HTLs.

PEDOT:PSS reduces the acidity of sulfur in PSS as mentioned in Figure 2 (water contact angle measurement and XPS measurements), suggesting that two-component PEDOT:PSS/2PACz is less directly affected, thereby improving the operational and shelf-life stability.

Finally, to examine the applicability and generality of two-component PEDOT:PSS/2PACz HTLs, we tested various other NFA systems including PM6:Y6, PM6:ITIC-4F, PM6:BTP-eC9:PC$_{71}$BM, PM6:BTP-eC9:ITIC-4F, and PM6:Y6 (no additive). Indeed, we find that the OSCs with two-component PEDOT:PSS/2PACz HTL generally exhibits higher PCEs in comparison to OSCs with PEDOT:PSS HTLs (see Figure S13, Supporting Information). This demonstrates that a better interfacial region at the HTL/BHJ interface is achieved, resulting in a generally improved device performance, for OSCs using a two-component PEDOT:PSS/2PACz HTL. We further note that electrode-induced doping of the active layer has also been observed to occur with other transport layers in different BHJ systems.[57–60] As such, we expect that our findings are not limited to PEDOT:PSS but may also be applicable to other HTLs as well.

3. Conclusion

In summary, we present a simple approach to improve the device performance by introducing a 2PACz SAM layer at the interface between PEDOT:PSS and the BHJ active layer based on PM6:BTP-eC9 and various other NFA-based OSC systems. The results from XPS measurements show that the O atoms in 2PACz can chemically interact with the S atoms in PEDOT:PSS, resulting in a better contact with less formation of pinholes and defects. Further, the overlaid 2PACz on PEDOT:PSS can effectively passivate the PSS$^-$ and the formation of a PSS$^-$ rich intermixed region, thus reducing photocurrent losses caused by non-geminate recombination. This results not only in an improved PCE of 17.7%, compared to the PCE of 17.1% for PEDOT:PSS, but also enhanced reproducibility with a narrow PCE distribution. In addition, our approach allows for longer device lifetimes under operation stability and shelf-life time stability, although these aspects need to be further explored with larger data sets with manufacturability in mind.

4. Experimental Section

Chemical Definitions: All materials were used as received. Poly(3,4-ethylenedioxythiophene) polystyrene sulfonate (PEDOT:PSS); poly[(2,6-(4,8-bis(5-(2-ethylhexyl-3-fluoro)thiophen-2-yl)-benzo[1,2-b:4,5-b′]dithiophene))-alt-(5,5-(1′,3′-di-2-thienyl-5′,7′-bis(2-ethylhexyl)benzo[1′,2′-c:4′,5′-c′]dithiophene-4,8-dione)] (PM6); 2,2′- [[12,13-Bis(2-butyloctyl)-12,13-dihydro-3,9-dinonylbisthieno[2″″,3″″:4″,5″]thieno[2″,3″:4,5]pyrrolo[3,2-e:2″,3″-g][2,1,3]benzothiadiazole-2,10-diyl]bis[methylidyne(5,6-chloro-3-oxo-1H-indene-2,1(3H)-diylidene)]]bis[propanedinitrile] (BTP-eC9); 2,2″-((2Z,2″Z)-((12,13-bis(2-ethylhexyl)-3,9-diundecyl-12,13-dihydro-[1,2,5]thiadiazolo[3,4-e]thieno[2",3’″:4’,5″]thieno[2″,3″:4,5]pyrrolo[3,2-g]thieno[2″,3″:4,5]thieno[3,2-b]indole-2,10-diyl)bis(methanylylidene))bis(5,6-difluoro-3-oxo-2,3-dihydro-1H-indene-2,1-diylidene))dimalononitrile (Y6); 3,9-bis(2-methylene-((3-(1,1-dicyanomethylene)-6,7-difluoro)-indanone))-5,5,11,11-tetrakis(4-hexylphenyl)-dithieno[2,3-d:2’,3’-d’]-s-indaceno[1,2--b:5,6-b’]dithiophene (ITIC-4F), [6,6]-Phenyl-C71-butyric acid methyl ester (PC71BM), Poly[[2,7-bis(2-ethylhexyl)-1,2,3,6,7,8-hexahydro-1,3,6,8-tetraoxobenzo[lmn][3,8]phenanthroline-4,9-diyl]-2,5-thiophenediyl[9,9-bis[3’((N,N-dimethyl)-N-ethylammonium)]-propyl]-9H-fluorene-2,7-diyl]-2,5-thiophenediyl] (PNDIT-F3N-Br); [2-(9H-Carbazol-9-yl)ethyl]phosphonic Acid (2PACz);

Materials: PEDOT:PSS (Clevios AI 4083) was purchased from Heraeus. PM6, ITIC-4F, Y6 and BTP-eC9 were purchased from Solarmer in China. PC$_{71}$BM was purchased from Ossila. PNDIT-F3N-Br was purchased from 1-Materials. Indium tin oxide substrate (ITO) was purchased from the AMG tech company. 1,8-diiodooctane (DIO), 1-chloronaphthalene (CN), isopropyl alcohol (IPA), acetone, ethanol (EtOH), and chloroform were purchased from Sigma–Aldrich. 2PACz was purchased from TCI Chemicals.

Substrate Preparation: Commercial patterned ITO substrates were cleaned with detergent, deionized (DI) water, acetone, and IPA by sequential sonication for 15 min. The cleaned substrates were first dried by nitrogen and then kept in a hot oven (80 °C) overnight. Afterward, the dried and cleaned substrates were treated in a UV-Ozone cleaner (Ossila, L2002A2-UK) for 30 min before the deposition of hole transport layer.

Device Fabrication: PM6:BTP-eC9 devices were fabricated in a dry nitrogen glove box with a conventional structure (ITO/PEDOT:PSS or PEDOT:PSS/2PACz /PM6:BTP-eC9/PNDIT-F3N-Br/Ag). PM6:BTP-eC9 was dissolved in a CF:DIO (the volume ratio of 99.5:0.5) solution with a weight ratio 1:1.2 (donor:acceptor) by weight (17 mg mL^{-1}), PM6:Y6 was dissolved in a CF:CN (the volume ratio of 99.5:0.5) solution with a weight ratio 1:1.2 (donor:acceptor) by weight (17 mg mL^{-1}), PM6:ITIC-4F was dissolved in a CF:DIO (the volume ratio of 99.5:0.5) solution with a weight ratio 1:1 (donor:acceptor) by weight (17 mg mL^{-1}).

PM6:BTP-eC9:ITIC-4F was dissolved in a CF:DIO (the volume ratio of 99.5:0.5) solution with a weight ratio 1:1.1:0.1 (donor:acceptor:acceptor) by weight (17 mg mL^{-1}), PM6:BTP-eC9:PC$_{71}$BM was dissolved in a CF:DIO (the volume ratio of 99.5:0.5) solution with a weight ratio 1:1.1:0.1 (donor:acceptor:acceptor) by weight (17 mg mL^{-1}), resulting in the film thickness of ≈100 nm at 3500 rpm by dynamic spin-coating. Afterward, the films were thermally annealed at 90 °C for 10 min and 0.5 mg mL^{-1} of PNDIT-F3N-Br solution was spin-coated on PM6: BTP-eC9 film at 5000 rpm to form <10 nm films. The Ag electrode (100 nm) was thermally evaporated through a mask under a vacuum of ≈1×10^{-6} mbar, resulting in the pixel of 0.105 cm^2. The film thicknesses of all the above films were measured by ellipsometry. The samples were finally encapsulated under glass. The hole only device was finished by thermally evaporating a layer of 10 nm of MoO$_x$ and 100 nm of Ag electrode as top contract.

Device Characterization—Light and Dark Current Density–Voltage (J–V) Measurements: The J–V curves of the devices (pixel area: 0.105 cm^2) were measured through an illumination mask area of 0.036 cm^2 using an Ossila Solar Cell I-V Test System. The solar simulator was calibrated by a standard silicon reference cell certified by the National Renewable Energy Laboratory (KG5). Dark J–V curves were measured by a Keithley source-measure unit (model 2450).

Device Characterization—Charge Extraction by Linearly Increasing Voltage (CELIV): CELIV triangle voltage pulses were generated by a waveform function generator (Keysight, 33500B) and applied to the device under test (DUT). An oscilloscope (Rohde & Schwarz, RTM 3004) with a 25 Ω load resistance was used to record the CELIV transients. A ramp up rate of 1 V per 10 µs was applied to the DUT in the reverse bias and the corresponding current was measured in the dark.

Device Characterization—Photovoltaic External Quantum Efficiency (EQE_{PV}): For EQE_{PV} measurements, a spectrophotometer (PerkinElmer, Lambda 950) was used as a light source. The probe light was physically chopped at 273 Hz. No bias voltage was applied on the DUT during the measurement. Before recording the DUT response by a lock-in amplifier (Stanford Research, SR 860), the photocurrent signal was amplified by a current pre-amplifier (Femto, DLPCA-200). A NIST-calibrated Silicon photodiode sensor (Newport, 818-UV) was used to calibrate the EQE system before measurement. Detailed information of the EQE_{PV} apparatus has been provided elsewhere.[62]

Device Characterization—Electroluminescent External Quantum Efficiency (EQE_{EL}): EQE_{EL} was measured using a Hamamatsu EL measurement system (C9920-12). Here, the DUT was mounted into an integrating sphere, while a source-meter unit (Keithley 2450) was used to drive the DUT electroluminescence. A photonic multi-channel analyzer (PMA) (Hamamatsu, model: C10027-02) was used to record the EL spectra for wavelengths between 346 and 1100 nm. For calibration and EQE_{EL} calculations, proprietary software (Hamamatsu, U6039-06 Version 4.0.1) was used.

Device Characterization—Kelvin Probe Force Microscopy (KPFM): The surface potentials of films on ITO substrates were measured using a Bruker Dimension ICON XR scanning probe system. PFQNE-AL (Bruker) tips were used, and the system was operated in its PeakForce KPFM mode in tip biasing operation. Calibration of the work function of the probe was performed using a freshly cleaved HOPG surface, with a reference value of 4.48 eV.[61] Silver contacts were thermally evaporated around the edges of the ITO substrates prior to film deposition. These contacts were used to ground the samples to the stage during KPFM measurements. Analysis of the measured data was performed in the supplied Bruker software.

Device Characterization—X-Ray Photoelectron Spectroscopy (XPS): Chemical analysis of the deposited films was performed using a Kratos Axis Supra XPS (X-ray Photoelectron Spectroscopy) system with an Al Kα monochromatic source, with an emission current of 15 mA. The survey spectra were acquired with a pass energy of 160 eV. Narrow regions covering the C1s, O1s, N1s, S2p, P2p, and Sn 3d regions were collected with pass energy of 40 eV in FOV2(Field of View) lens mode. The samples were mounted electrically floating and charge compensation was achieved with a flood gun. The data analysis of the XPS measurements was performed using CasaXPS software (version 2.3.24rev1.1Z). Data were extracted using wide scan spectra, U3 Tougaard was used as a background for the measured data. An effective attenuation length was applied as an escape depth setting and the transition function was set to 1.

Device Characterization—UV Photoelectron Spectroscopy (UPS): UPS measurements of the samples were performed by using an NEXSA (Thermo Fisher Scientific) equipped with He-I radiation (21.22 eV) as a UV source and 1486.7 eV Al K- α radiation.

Device Characterization—Electro-Modulated-Photoluminescence Quantum Yield (EM-PLQY) Measurements: EM-PLQY measurements were performed in a manner described in detail in Ref. [54]. Prior to performing an EM-PLQY measurement, the sample was illuminated with a laser (custom-made 520 nm diode laser) and the short circuit current was measured. To perform the EM-PLQY measurements, the device was brought to open-circuit conditions where an applied time-dependent voltage (supplied by a Keysight 33500B function generator) was applied to the cell at angular frequency ω_V and amplitude ΔV. This results in a time-dependent injected current of amplitude ΔJ, which was measured on an oscilloscope (Rohde & Schwarz RTM3004). The emitted photoluminescence was filtered to remove any pump light (Thorlabs FEL 600550550), collected with an amplified photodiode (FEMTO OE-300-Si-30), and the amplitude ($\Delta\Phi$) was measured on a lock-in amplifier (Stanford Research Systems SR860) referenced to ω_V . The electro-modulated photoluminescence quantum yield could be calculated as $\eta_{EMPL} = \frac{q\Delta\Phi}{\Delta J}$. To evaluate η_{EMPL} at conditions close to open-circuit 1 sun illumination the laser power was adjusted such that the short-circuit current equals $J_{sc}^{AM1.5}$, leading V_{off} to be approximately $V_{oc}^{AM1.5}$. As this experiment suffers from reductions in geometric and spectral light collection efficiency of the system was calibrated using electroluminescence quantum yield experiments, reference to an absolute measurement system (Hamamatsu C9920-12) for each device.

Device Characterization—Operational Stability Measurements: The encapsulated devices were placed into a home-made chamber with a black cupboard for performance monitoring under continuous illumination in air. A white LED array was used as the light source with the intensity of the LED array and the device position adjusted such that the J_{sc} was approximately equal to that measured under 1 sun air mass (AM1.5G) illumination.

Device Characterization—Shelf-Life Time Stability Measurements: The encapsulated devices were stored in the dark at ambient conditions (in air).

Supporting Information

Supporting Information is available from the Wiley Online Library or from the author.

Acknowledgements

This work was supported by the Welsh Government's Sêr Cymru II Program through the European Regional Development Fund, Welsh European Funding Office, and Swansea University strategic initiative in Sustainable Advanced Materials. A.A. is a Sêr Cymru II Rising Star Fellow and P.M. is a Sêr Cymru II National Research Chair. This work was also funded by UKRI through the EPSRC Program Grant EP/T028511/1 Application Targeted Integrated Photovoltaics.

Conflict of Interest

The authors declare no conflict of interest.

Data Availability Statement

The data that support the findings of this study are available from the corresponding author upon reasonable request.

Keywords

hole transport layer, interfacial doping, interfacial recombination, organic solar cells

Received: January 5, 2023

[1] P. Bi, S. Zhang, Z. Chen, Y. Xu, Y. Cui, T. Zhang, J. Ren, J. Qin, L. Hong, X. Hao, J. Hou, *Joule* **2021**, *5*, 2408.
[2] Y. Cui, Y. Xu, H. Yao, P. Bi, L. Hong, J. Zhang, Y. Zu, T. Zhang, J. Qin, J. Ren, Z. Chen, C. He, X. Hao, Z. Wei, J. Hou, *Adv. Mater.* **2021**, *33*, 2102420.
[3] Z. Zheng, J. Wang, P. Bi, J. Ren, Y. Wang, Y. Yang, X. Liu, S. Zhang, J. Hou, *Joule* **2022**, *6*, 171.
[4] L. Zhu, M. Zhang, J. Xu, C. Li, J. Yan, G. Zhou, W. Zhong, T. Hao, J. Song, X. Xue, Z. Zhou, R. Zeng, H. Zhu, C.-C. Chen, R. C. I. MacKenzie, Y. Zou, J. Nelson, Y. Zhang, Y. Sun, F. Liu, *Nat. Mater.* **2022**, *21*, 656.
[5] J. Yuan, Y. Zhang, L. Zhou, G. Zhang, H.-L. Yip, T.-K. Lau, X. Lu, C. Zhu, H. Peng, P. A. Johnson, M. Leclerc, Y. Cao, J. Ulanski, Y. Li, Y. Zou, *Joule* **2019**, *3*, 1140.
[6] Y. Cui, H. Yao, J. Zhang, K. Xian, T. Zhang, L. Hong, Y. Wang, Y. Xu, K. Ma, C. An, C. He, Z. Wei, F. Gao, J. Hou, *Adv. Mater.* **2020**, *32*, 1908205.
[7] X.-K. Chen, D. Qian, Y. Wang, T. Kirchartz, W. Tress, H. Yao, J. Yuan, M. Hülsbeck, M. Zhang, Y. Zou, Y. Sun, Y. Li, J. Hou, O. Inganäs, V. Coropceanu, J.-L. Bredas, F. Gao, *Nat. Energy* **2021**, *6*, 799.
[8] A. Armin, W. Li, O. J. Sandberg, Z. Xiao, L. Ding, J. Nelson, D. Neher, K. Vandewal, S. Shoaee, T. Wang, H. Ade, T. Heumüller, C. Brabec, P. Meredith, *Adv. Energy Mater.* **2021**, *11*, 2003570.
[9] W. Li, S. Zeiske, O. J. Sandberg, D. B. Riley, P. Meredith, A. Armin, *Energy Environ. Sci.* **2021**, *14*, 6484.
[10] S. M. Hosseini, N. Tokmoldin, Y. W. Lee, Y. Zou, H. Y. Woo, D. Neher, S. Shoaee, *Solar RRL* **2020**, *4*, 2000498.
[11] J. Yao, B. Qiu, Z.-G. Zhang, L. Xue, R. Wang, C. Zhang, S. Chen, Q. Zhou, C. Sun, C. Yang, M. Xiao, L. Meng, Y. Li, *Nat. Commun.* **2020**, *11*, 2726.
[12] J. Yao, Q. Chen, C. Zhang, Z.-G. Zhang, Y. Li, *SusMat* **2022**, *2*, 243.
[13] Y. Lin, Y. Firdaus, F. H. Isikgor, M. I. Nugraha, E. Yengel, G. T. Harrison, R. Hallani, A. El-Labban, H. Faber, C. Ma, X. Zheng, A. Subbiah, C. T. Howells, O. M. Bakr, I. McCulloch, S. D. Wolf, L. Tsetseris, T. D. Anthopoulos, *ACS Energy Lett.* **2020**, *5*, 2935.
[14] Y. Lin, A. Magomedov, Y. Firdaus, D. Kaltsas, A. El-Labban, H. Faber, D. R. Naphade, E. Yengel, X. Zheng, E. Yarali, N. Chaturvedi, K. Loganathan, D. Gkeka, S. H. AlShammari, O. M. Bakr, F. Laquai, L. Tsetseris, V. Getautis, T. D. Anthopoulos, *ChemSusChem* **2021**, *14*, 3569.
[15] L. Ding, M. Jonforsen, L. S. Roman, M. R. Andersson, O. Inganäs, *Synth. Met.* **2000**, *110*, 133.
[16] M. Lefebvre, Z. Qi, D. Rana, P. G. Pickup, *Chem. Mater.* **1999**, *11*, 262.
[17] X. Fan, W. Nie, H. Tsai, N. Wang, H. Huang, Y. Cheng, R. Wen, L. Ma, F. Yan, Y. Xia, *Adv. Sci.* **2019**, *6*, 1900813.
[18] M. P. de Jong, L. J. van IJzendoorn, M. J. A. de Voigt, *Appl. Phys. Lett.* **2000**, *77*, 2255.
[19] N. Wijeyasinghe, A. Regoutz, F. Eisner, T. Du, L. Tsetseris, Y.-H. Lin, H. Faber, P. Pattanasattayavong, J. Li, F. Yan, M. A. McLachlan, D. J. Payne, M. Heeney, T. D. Anthopoulos, *Adv. Funct. Mater.* **2017**, *27*, 1701818.
[20] K. Sun, S. Zhang, P. Li, Y. Xia, X. Zhang, D. Du, F. H. Isikgor, J. Ouyang, *J. Mater. Sci.: Mater. Electron.* **2015**, *26*, 4438.
[21] A. Garcia, G. C. Welch, E. L. Ratcliff, D. S. Ginley, G. C. Bazan, D. C. Olson, *Adv. Mater.* **2012**, *24*, 5368.
[22] H. Peisert, M. Knupfer, F. Zhang, A. Petr, L. Dunsch, J. Fink, *Appl. Phys. Lett.* **2003**, *83*, 3930.
[23] F. Ma, Y. Zhao, J. Li, X. Zhang, H. Gu, J. You, *J. Energy Chem.* **2021**, *52*, 393.
[24] K. Wang, Y. Shi, Q. Dong, Y. Li, S. Wang, X. Yu, M. Wu, T. Ma, *J. Phys. Chem. Lett.* **2015**, *6*, 755.
[25] Z. Ni, S. Ding, H. Zhang, R. Dai, A. Chen, R. Wang, J. Zhang, Y. Zhou, J. Yang, T. Sun, *Adv. Mater. Interfaces* **2022**, *9*, 2200812.
[26] T. Ki, C. Lee, J. Kim, I. W. Hwang, C. M. Oh, K. Park, S. Lee, J. H. Kim, C. Balamurugan, J. Kong, *Adv. Funct. Mater.* **2022**, *32*, 2204493.
[27] H. N. Tran, H. Lee, C. B. Park, N. V. Krishna, F. T. A. Wibowo, S. Y. Jang, J. Y. Kim, S. Cho, *Adv. Mater. Interfaces* **2022**, *9*, 2201274.
[28] L. Chen, Q. Xie, L. Wan, W. Zhang, S. Fu, H. Zhang, X. Ling, J. Yuan, L. Miao, C. Shen, X. Li, W. Zhang, B. Zhu, H.-Q. Wang, *ACS Appl. Energy Mater.* **2019**, *2*, 5862.
[29] H. N. Tran, S. Park, F. T. A. Wibowo, N. V. Krishna, J. H. Kang, J. H. Seo, H. Nguyen-Phu, S.-Y. Jang, S. Cho, *Adv. Sci.* **2020**, *7*, 2002395.
[30] A. Al-Ashouri, A. Magomedov, M. Roß, M. Jošt, M. Talaikis, G. Chistiakova, T. Bertram, J. A. Márquez, E. Köhnen, E. Kasparavičius, S. Levcenco, L. Gil-Escrig, C. J. Hages, R. Schlatmann, B. Rech, T. Malinauskas, T. Unold, C. A. Kaufmann, L. Korte, G. Niaura, V. Getautis, S. Albrecht, *Energy Environ. Sci.* **2019**, *12*, 3356.
[31] A. Al-Ashouri, E. Köhnen, B. Li, A. Magomedov, H. Hempel, P. Caprioglio, J. A. Márquez, A. B. M. Vilches, E. Kasparavicius, J. A. Smith, N. Phung, D. Menzel, M. Grischek, L. Kegelmann, D. Skroblin, C. Gollwitzer, T. Malinauskas, M. Jošt, G. Matič, B. Rech, R. Schlatmann, M. Topič, L. Korte, A. Abate, B. Stannowski, D. Neher, M. Stolterfoht, T. Unold, V. Getautis, S. Albrecht, *Science* **2020**, *370*, 1300.
[32] S. Gharibzadeh, P. Fassl, I. M. Hossain, P. Rohrbeck, M. Frericks, M. Schmidt, M. R. Khan, T. Abzieher, B. A. Nejand, F. Schackmar, *Energy Environ. Sci.* **2021**, *14*, 5875.
[33] B. A. Nejand, D. B. Ritzer, H. Hu, F. Schackmar, S. Moghadamzadeh, T. Feeney, R. Singh, F. Laufer, R. Schmager, R. Azmi, *Nat. Energy* **2022**, *7*, 620.
[34] L. Mao, T. Yang, H. Zhang, J. Shi, Y. Hu, P. Zeng, F. Li, J. Gong, X. Fang, Y. Sun, X. Liu, J. Du, A. Han, L. Zhang, W. Liu, F. Meng, X. Cui, Z. Liu, M. Liu, *Adv. Mater.* **2022**, *34*, 2206193.
[35] J. Liu, M. de Bastiani, E. Aydin, G. T. Harrison, Y. Gao, R. R. Pradhan, M. K. Eswaran, M. Mandal, W. Yan, A. Seitkhan, M. Babics, A. S. Subbiah, E. Ugur, F. Xu, L. Xu, M. Wang, A. U. Rehman, A. Razzaq, J. Kang, R. Azmi, A. A. Said, F. H. Isikgor, T. G. Allen, D. Andrienko, U. Schwingenschlögl, F. Laquai, S. de Wolf, *Science* **2022**, *377*, 302.
[36] F. H. Isikgor, F. Furlan, J. Liu, E. Ugur, M. K. Eswaran, A. S. Subbiah, E. Yengel, M. de Bastiani, G. T. Harrison, S. Zhumagali, C. T. Howells, E. Aydin, M. Wang, N. Gasparini, T. G. Allen, A. U. Rehman, E. van Kerschaver, D. Baran, I. McCulloch, T. D. Anthopoulos, U. Schwingenschlögl, F. Laquai, S. de Wolf, *Joule* **2021**, *5*, 1566.
[37] M. D. Losego, J. T. Guske, A. Efremenko, J.-P. Maria, S. Franzen, *Langmuir* **2011**, *27*, 11883.
[38] M. Chockalingam, N. Darwish, G. L.e Saux, J. J. Gooding, *Langmuir* **2011**, *27*, 2545.
[39] R. T. Hassarati, J. A. Goding, S. Baek, A. J. Patton, L. A. Poole-Warren, R. A. Green, *J. Polym. Sci., Part B: Polym. Phys.* **2014**, *52*, 666.
[40] S. Kim, Y. Lee, M. Lee, S. An, S.-J. Cho, *Nanomaterials* **2021**, *11*, 1593.
[41] S. Heutz, R. Cloots, T. S. Jones, *Appl. Phys. Lett.* **2000**, *77*, 3938.
[42] K. Eguchi, C. Nanjo, K. Awaga, H.-H. Tseng, P. Robaschik, S. Heutz, *Phys. Chem. Chem. Phys.* **2016**, *18*, 17360.
[43] S.-M. Kim, C.-H. Kim, Y. Kim, N. Kim, W.-J. Lee, E.-H. Lee, D. Kim, S. Park, K. Lee, J. Rivnay, M.-H. Yoon, *Nat. Commun.* **2018**, *9*, 3858.
[44] N. Massonnet, A. Carella, A. de Geyer, J. Faure-Vincent, J.-P. Simonato, *Chem. Sci.* **2015**, *6*, 412.
[45] M. Chen, G. Kapil, L. Wang, S. R. Sahamir, A. K. Baranwal, K. Nishimura, Y. Sanehira, Z. Zhang, M. A. Kamarudin, Q. Shen, S. Hayase, *Chem. Eng. J.* **2022**, *436*, 135196.
[46] O. J. Sandberg, M. Nyman, R. Österbacka, *Phys. Rev. Appl.* **2014**, *1*, 024003.

[47] S. Zeiske, O. J. Sandberg, N. Zarrabi, W. Li, P. Meredith, A. Armin, *Nat. Commun.* **2021**, *12*, 3603.

[48] J. Reinhardt, M. Grein, C. Bühler, M. Schubert, U. Würfel, *Adv. Energy Mater.* **2014**, *4*, 1400081.

[49] S. Wheeler, F. Deledalle, N. Tokmoldin, T. Kirchartz, J. Nelson, J. R. Durrant, *Phys. Rev. Appl.* **2015**, *4*, 024020.

[50] A. Sundqvist, O. J. Sandberg, M. Nyman, J.-H. Smått, R. Österbacka, *Adv. Energy Mater.* **2016**, *6*, 1502265.

[51] G. Juška, K. Arlauskas, M. Viliūnas, J. Kočka, *Phys. Rev. Lett.* **2000**, *84*, 4946.

[52] G. Juška, K. Arlauskas, M. Viliūnas, K. Genevičius, R. Österbacka, H. Stubb, *Phys. Rev. B* **2000**, *62*, R16235.

[53] M. Nyman, O. J. Sandberg, S. Dahlström, D. Spoltore, C. Körner, Y. Zhang, S. Barlow, S. R. Marder, K. Leo, K. Vandewal, R. Österbacka, *Sci. Rep.* **2017**, *7*, 5397.

[54] D. B. Riley, O. J. Sandberg, N. M. Wilson, W. Li, S. Zeiske, N. Zarrabi, P. Meredith, R. Österbacka, A. Armin, *Phys. Rev. Appl.* **2021**, *15*, 064035.

[55] T. Kirchartz, T. Agostinelli, M. Campoy-Quiles, W. Gong, J. Nelson, *J. Phys. Chem. Lett.* **2012**, *3*, 3470.

[56] O. J. Sandberg, S. Dahlström, M. Nyman, S. Wilken, D. Scheunemann, R. Österbacka, *Phys. Rev. Appl.* **2019**, *12*, 034008.

[57] M. Nyman, S. Dahlström, O. J. Sandberg, R. Österbacka, *Adv. Energy Mater.* **2016**, *6*, 1600670.

[58] S. Torabi, J. Liu, P. Gordiichuk, A. Herrmann, L. Qiu, F. Jahani, J. C. Hummelen, L. J. A. Koster, *ACS Appl. Mater. Interfaces* **2016**, *8*, 22623.

[59] J. Wang, L. Xu, B. Zhang, Y.-J. Lee, J. W. P. Hsu, *Adv. Electron. Mater.* **2017**, *3*, 1600458.

[60] A. Dai, A. Wan, C. Magee, Y. Zhang, S. Barlow, S. R. Marder, A. Kahn, *Org. Electron.* **2015**, *23*, 151.

[61] C. Melios, A. Centeno, A. Zurutuza, V. Panchal, C. E. Giusca, S. Spencer, S. R. P. Silva, O. Kazakova, *Carbon* **2016**, *103*, 273.

[62] C. Zeiske, C. Kaiser, P. Meredith, A. Armin, Sensitivity of Sub-Bandgap External Quantum Efficiency Measurements of Solar Cells under Electrical and Light Bias. ACS Photonics, **2019**, pp. 256–264. https://doi.org/10.1021/acsphotonics.9b01531